Journal of
Materials Chemistry A

PAPER

View Article Online
View Journal

Cite this: DOI: 10.1039/c7ta07332a

In situ probing of interfacial kinetics for studying the electrochemical properties of active nano/micro-particles and the state of Li-ion batteries†

Wenju Ren, Haibiao Chen, Rongxue Qiao, Yuan Lin* and Feng Pan *

It is critical to monitor the state of health (SOH) of the Li-ion batteries to ensure a safe operation and to extend the service life of the batteries in electric vehicles. In this work, we demonstrated that the equivalent capacitance (C_p) and resistance (R_p) of the electrode interface derived using a first-order RC equivalent circuit under a large galvanostatic pulse (LGPM) condition can be correlated with SOH. For both the cathode and the anode, the interfacial kinetics of Li-ions were analyzed to study the electrochemical properties of active particles. The RC parameters of the equivalent circuit were correlated with the diffusion kinetics of Li-ions near the interface between the electrolyte and the active nano/micro-particles during fast charging/discharging. For fresh $LiFePO_4$ (LFP)/Li half-cells, the values and the change of C_p and R_p were explained using the hypothesis of interparticle ion transport under a non-equilibrium condition. For graphite/Li half-cells, the buffering of Li-ions by the solid-electrolyte interphase (SEI) layer was speculated to affect C_p and R_p under a non-equilibrium condition. In commercial LFP/graphite batteries, the C_p values of unhealthy batteries were found to be higher than those of healthy batteries. In further tests, the C_p values of the half cells with the graphite anode recovered from the unhealthy batteries were found to be higher than those of the half cells with graphite from the healthy batteries. The half cells with LFP from the unhealthy batteries behaved similarly to those with LFP from the healthy batteries. With additional analysis on the microstructure, we proposed that the deterioration of the LFP/graphite batteries was mostly due to the formation of a thicker SEI on the graphite anode. The method developed in this work can be integrated in EVs at a low calculation cost. More importantly, we gained a better understanding of the interfacial kinetics of Li-ions during a non-equilibrium process.

Received 19th August 2017
Accepted 3rd October 2017

DOI: 10.1039/c7ta07332a

rsc.li/materials-a

Introduction

The emerging large-scale applications of lithium-ion batteries (LIBs) in transportation have imposed more strict requirements on the performance, service life, cost, and safety.[1] For LIBs, the lifetime cost is largely determined by the length of the service life, which should be extended as much as possible by properly managing the operation of the batteries. An effective battery management system (BMS) should be able to avoid premature failures and accidents. A key function of the BMS is to closely monitor the status of the battery during operation, by determining the state of health (SOH) and the state of charge (SOC) in real time.[2–17] Due to complex electrochemical and physical processes taking place during the operation of LIBs, it is challenging to correctly determine the SOH and SOC based on limited real-time measurements, such as current and voltage.[2–5] The situation gets especially complicated in electric vehicles (EVs), where the batteries constantly experience a dynamic process consisting of intermittent charge and discharge pulses depending on the driving conditions. In recent years, there have been many reported studies to develop health models and methods for estimating the SOH of LIBs.[5–11] The electrochemistry models and the equivalent circuit models are the most commonly studied categories. Detailed electro-chemistry models are generally not suitable for online use due to their complexity.[12–16] In contrast, equivalent circuit models built on electronic components can be described using simple mathematical formulas, and they are more viable for the real-time analysis and management of the batteries in EVs.[17–24] Nevertheless, complicated equivalent circuit models can also be built to achieve highly accurate results.[25,26] However, complicated models are demanding on hardware resource and computing capabilities and tend to cause system instability. In order to accurately determine the SOH using a simple algorithm, a model needs to be developed to correctly correlate the response of *in situ* measurements with the material structures,

---

School of Advanced Materials, Peking University, Shenzhen Graduate School, Shenzhen, 518055, People's Republic of China. E-mail: panfeng@pkusz.edu.cn; linyuan@iccas.ac.cn

† Electronic supplementary information (ESI) available. See DOI: 10.1039/c7ta07332a

the interfacial kinetics of Li-ion transport, and the degradation of LIBs.

Common cathode materials in commercial LIBs include layered oxides (such as $LiNi_{1-x-y}Mn_xCo_yO_2$ (NMC) and $LiNi_{0.8}Co_{0.15}Al_{0.05}O_2$ (NCA)), doped lithium manganese oxide spinel ($LiMn_2O_4$) and $LiFePO_4$ (LFP), and the most common anode materials include graphite and lithium titanate ($Li_4Ti_5O_{12}$, LTO) spinels.[27] Due to the low material cost, excellent cycle life, and high safety level, LFP/graphite batteries are gaining a large share in the EV market. The flat charge and discharge voltage platforms of the LFP/graphite batteries make it difficult to correctly estimate the SOH and SOC using simple algorithms. In order to properly manage the batteries for EVs, understanding the properties of individual particles and the inter-particle interaction in cathode/anode electrodes is important. In our previous work, the intrinsic properties and performance of the nano-sized single-particles (SPs) of LFP were investigated by creating the SP electrode and developing the SP electrochemical model to get insight into the Li-ion diffusion and the interfacial kinetics during charging–discharging. When nano-sized single-particles were assembled together to create electrodes, it was found that the solution diffusion, effective porosity, and electrode thickness can dominate the high rate performance, which was demonstrated in the 3D-printed and traditional $LiMn_{0.21}Fe_{0.79}PO_4$ electrodes for Li-ions batteries.[28] Hence, in order to get better understanding of the Li-ion transport kinetics at the electrode interfaces and the degradation mechanism of full Li-ion batteries for EV, a new method needs to be developed for *in situ* probing the behaviors of the Li-ions (such as ionic concentration, diffusion/reaction rate and effective activation area) related to the nano/micro-particles of cathode/anode active materials during charging–discharging.

In this work, we developed a simple first-order RC equivalent circuit to model LFP/graphite half-cells and full batteries and to fit the voltage response during a designed large galvanostatic pulse method (LGPM). By applying a large step current (1 C) to create a state far from equilibrium, the equivalent capacitance was derived and was related to the Li-ion transport kinetics around the interfaces during the charge–discharge process. Note that the LGPM is different from the traditional galvanostatic intermittent titration technique (GITT) and potentiostatic intermittent titration technique (PITT) methods, which are mainly used to measure the Li-ion diffusion coefficients near equilibrium in bulk crystals by applying low-magnitude pulses. In the tests of fresh LFP/Li and graphite/Li half cells, LFP nanoparticles demonstrated 3–4 times higher equivalent capacitance than graphite microparticles with equal lithium capacity, likely resulting from the nano-sized LFP particles having a much larger effective surface area than micro-scale graphite. By separately testing the half-cells assembled using the electrodes from the full-batteries with different SOHs, we were able to identify that the change of the graphite anode in the battery took more responsibility for the deteriorated SOH. By testing full batteries with different SOHs and verifying the relevant morphology of the electrodes by *ex situ* examination, we were able to correlate the value of the equivalent capacitance with the SOH of the electrodes and full batteries. From these results, we gained a clearer understanding of the degradation mechanism of LFP/graphite batteries. With further optimizations, the LGPM can become a promising *in situ* protocol for monitoring the SOH of LIBs with high accuracy, and it will be especially practical for the power systems in EVs. In an actual system, the voltage response curve can be measured when the automobile is starting or accelerating, and the value of equivalent capacitance can be calculated using an on-board programmed microcontroller unit (MCU) and converted to a specific SOH value in real time.

The LGPM test and analysis on the RC model and the interface

The LGPM consists of a series of 1 C charge or discharge pulses, and each pulse lasts 10 seconds followed by a resting period of 30 seconds, as shown in Fig. 1a. The full discharge and charge profile can be seen in Fig. S1 and S2.† When a large step current is applied to discharge the battery, there is an immediate voltage drop as shown by the marked section (a, b) in Fig. 1a. In the following seconds, the voltage continues to drop at a much slower rate, as shown by the marked section (b, c) in Fig. 1a. To fit the voltage response in the section (b, c), both first-order and second-order RC equivalent circuits were applied. Comparison between the results using these two circuits can be seen in Fig. S3, Tables S1 and S2.† Compared to the second-order RC equivalent circuit, the first-order RC equivalent circuit could fit the voltage response curve with satisfactory accuracy and required less computation. Thus, the voltage response in the section (b, c) was fitted using the first-order RC equivalent circuit in this work, as shown in Fig. 1b and c.

During charging or discharging, four fundamental electrochemical procedures are taking place, which are capacitor charging, charge transfer, mass transport, and ion migration.[29] As soon as a current starts to flow, the voltage will immediately change due to the ohmic polarization, and a serial resistor (R_s) can be used to simulate the sudden voltage drop in the section (a, b) in Fig. 1a. R_s is mostly contributed by the resistance of the bulk electrolyte. According to Ohm's law, the value of R_s in the equivalent circuit shown in Fig. 1c could be calculated using eqn (1).

$$R_s = U_1/I \tag{1}$$

U_1 is the voltage drop in the section (a, b) and I is the current.

Then, the shunt capacitor (C_p) starts to receive charge and simultaneously charge transfer starts to take place as if current flows through another resistor in parallel (R_p). C_p and R_p are used to simulate the behaviour of the electrode/electrolyte interface. The total current (I) during the transient process is a constant and it equals to the sum of the capacitor charging current (I_c) and the faradic current through R_p (I_f). At the very beginning (t_0), charge transfer through the interface has not started ($I_f = 0$) and all charges are accumulating at the interface ($I_c = I$). As the current continues, the voltage will build up on C_p ($U_p = It/C_p$) and it drives charge transfer across the interface as accomplished by lithium insertion or extraction. As U_p goes

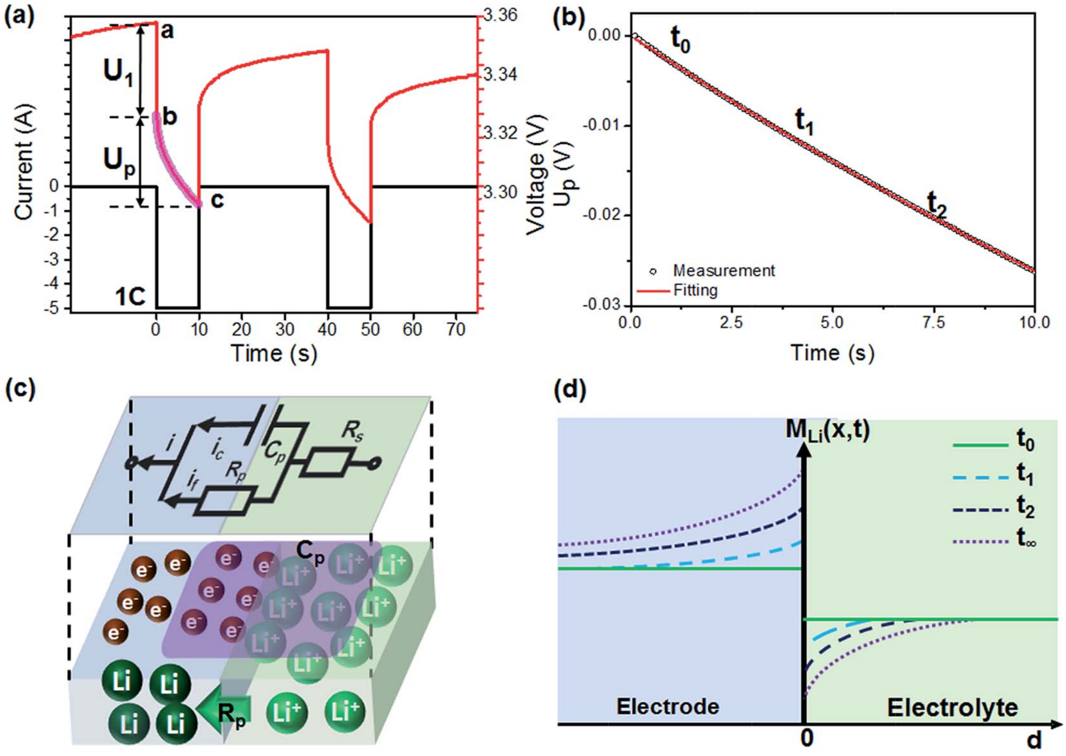

Fig. 1 (a) LGPM test and battery voltage response; (b) the voltage response curve and voltage curve fitting; (c) schematic diagram of charge transfer, double layer charge, diffusion mass transfer and ion/electron conduction between the electrode and electrolyte; (d) concentration profile of lithium ions at the interface between the electrode and the electrolyte as a function of time.

higher, more charges transfer through the interface as if the current flows through a constant resistor ($I_f = U_p/R_p$). Before reaching the steady state, *e.g.* at t_1 and t_2, the C_p charging current is gradually decreasing ($I_c\downarrow$) and the current to R_p is gradually increasing ($I_f\uparrow$). When the system reaches the steady state (at t_∞), the current is completely contributed by the charge transfer across the interface ($I_f = I$). Using this RC equivalent circuit, the values of R_p and C_p can be determined by fitting the voltage response curve during the transient state using eqn (2).

$$U_p = IR_p\left(1 - e^{\frac{-t}{R_pC_p}}\right) \qquad (2)$$

where U_p is the voltage on the RC circuit and it is converted from the measured voltage response, I is the current, and t is the time since the onset of current.

As we applied the LGPM to purposely create a transient state at the electrode/electrolyte interface, it is interesting to study the behaviour of the ions at the interface. When a large step current is supplied to an electrode, the concentration profile of Li-ions near the electrode/electrolyte interface changes with time, as schematically shown in Fig. 1d for the case of Li insertion. Before a current is applied (t_0), the concentration of Li-ions in both the electrode and the electrolyte can be assumed to be homogeneous. As the current starts, the difference between the concentrations of Li-ions on two sides of the interface becomes larger and larger (t_1 through t_2 in Fig. 1d), owing to the different diffusion rates of Li-ions in the solid electrode and liquid electrolyte during the mass transfer process. At the end of the transient state the concentration of Li-ions in the electrolyte at the surface of the electrode becomes minimal as all arriving Li-ions immediately enter the electrode (t_∞ in Fig. 1d), and the concentration of polarization reaches the maximum. Therefore, the rate determining step during the charge transfer process is the diffusion of Li in the solid electrode. Unlike the conditions used in traditional GITT, PITT or EIS under quasi-equilibrium conditions with galvanostatic pulses of low magnitude (about 0.05 to 0.1 C), the Li-ion transport kinetics at the electrode interfaces were now studied under high concentration polarization using galvanostatic pulses of a large current (1 C). In general, the transport of Li-ions in the electrolyte will be much faster than that in the solid electrodes. Thus, by the LGPM the transport of Li-ions at the surfaces and in the bulk of active materials of the electrodes can be investigated in depth at different SOCs during charging–discharging.

Experimental

Commercial graphite (Shenzhen BTR New Energy Technology Co., Ltd, Shenzhen, China) and commercial LFP (Shenzhen Dynanonic Co., Ltd, Shenzhen, China) were used to make fresh half-cells for validating the model. 2032-type coin cells were assembled in a glovebox filled with argon. Lithium pellets were used as the counter electrode, and 1 M $LiPF_6$ dissolved in ethylene carbonate/diethyl carbonate (EC/DEC) (3 : 7 by volume, Aladdin) was used as the electrolyte, and Celgard 2400 polypropylene was used as the separator. First, the cells were measured by galvanostatic charging–discharging for two cycles at 25 °C on a Neware CT4008 multichannel battery testing system. Commercial LFP-32650 batteries (size: 32 mm diameter × 65 mm height, cathode: $LiFePO_4$, anode: graphite, electrolyte: 1 M $LiPF_6$ dissolved in EC and DMC, rated capacity: 5 Ah, OptimumNano Energy Co., Ltd, Shenzhen, China) were used as full-batteries in the SOH study. The batteries were divided into two groups: healthy batteries (HB) with SOH > 90%, and unhealthy batteries (UB) with SOH < 80%. The value of SOH was calculated using eqn (3).

$$\mathrm{SOH} = C_{\mathrm{real}}/C_{\mathrm{rated}} \tag{3}$$

C_{real} is the actual capacity of the battery, and C_{rated} is the rated capacity of the battery which is 5 Ah at 0.1 C. Unhealthy batteries were obtained by intentionally cycling the new batteries for more than 1000 times until the SOH is below 80% using the working condition test.[30] Following the LGPM protocol, the commercial LFP-32650 batteries were tested on a high-speed pulse battery testing instrument (Maccor, MC16/MC4200) to get the voltage response curve. To analyse the change of the batteries with different SOHs, the values of the components in the RC equivalent circuit were calculated.

In order to analyse the change in the morphology of the electrodes, commercial LFP-32650 batteries with different SOHs were disassembled in the glovebox to remove the electrodes for *ex situ* characterization. Care was taken during battery disassembly to avoid accidental short circuit of the electrodes and the detailed procedure is provided in the ESI Section S1.† A 3D laser confocal scanning microscope (Keyence VK-X200) was used to observe the morphology and profile of the electrode surface. The surface roughness was quantified using the ISO 4287:1997 standard. The cross-sections of electrodes from batteries with different SOHs were prepared using a focused ion beam (FIB, FEI, Scios). The cross-sectional morphology and the structure were observed using field emission scanning electron microscopes (FE-SEM, ZEISS SUPRA®55 and FEI Scios). The anode and cathode were removed from commercial LFP-32650 batteries with different SOHs and were used to assemble 2032-type LFP/Li and graphite/Li half cells, which were tested using the LGPM to determine which electrode in a full battery was responsible for the degradation.

Results and discussion

In situ probing of interface of C_p and R_p and the Li-ion status of $LiFePO_4$ nanoparticles

Fresh LFP/Li half-cells, in which LFP nanoparticles were used as the cathode, were analyzed using the equivalent circuit model after the LGPM test. The equivalent capacitance (C_p) and the parallel resistance (R_p) of LFP/Li half-cells during charging and discharging were plotted as functions of SOC as shown in Fig. 2a and b (Fig. S10a and b†). Note that the C_p value was about 0.03–0.21 F, which was 1–2 orders of magnitude higher than the EDLC (only 0.0025 F) deduced using the surface area of the active material (detailed derivation can be found in the ESI Section S2†). Therefore the C_p value was mainly contributed by the effective interfacial area (indicated in Fig. 1c) due to the accumulation, diffusion and migration of the Li-ions on the interface between the electrode and the electrolyte under the condition of the LGPM.

Fig. 2a shows the C_p curve of LFP during the charge (delithiation) process, and there is a quick rise at the beginning (SOC < 10%) and a vast decline at the last part (SOC > 90%). However, the C_p value remains almost unchanged in the intermediate region (20–80%), which can be explained by the change in the effective surface area of LFP particles with a distribution of particle size. For LFP particles with a heterogeneous particle size distribution, the concentration of Li-ions within individual particles (or the ratio of $LiFePO_4/(LiFePO_4 + FePO_4)$) at electrochemical equilibrium depends on their particle size.[31] The electrochemical potential of Li-ions in smaller particles is lower so Li-ions will preferentially fill smaller particles when the system is at electrochemical equilibrium. When a large current was supplied to the LFP electrode, it caused a state far from equilibrium and significant polarization. As illustrated in Fig. 2c, a large delithiation current would drive Li-ions to extract from particles of all sizes and the effective surface area would be the total surface area independent of the SOC. Since the effective surface area remained almost constant during delithiation, the value of C_p should be constant during the delithiation process. There are two extreme cases when SOC was below 10% or higher than 90%, and C_p was lower. When SOC was from 100% to 90% (concentration of Li-ions from 100% to 90% in LFP), almost all particles were filled with Li-ions, and the driving force for Li extraction would be high and Li-ions would quickly extract from the particles without accumulation at the interface, causing C_p to rise. At SOC < 10%, almost all particles were void of Li-ions, and the lower concentration of Li-ions within the particles would lead to lower C_p.

During lithiation of the LFP electrode, the change of C_p as a function of the SOC can also be explained by the dependence of the state of lithiation on the particle size. At electrochemical equilibrium, smaller particles would be preferentially lithiated due to a lower electrochemical potential. Some smaller particles might be completely saturated at a given SOC. As illustrated in Fig. 2c, a large lithiation current would drive Li-ions to the external surface of particles which were not saturated. The effective surface area and the corresponding C_p were only determined by the non-saturated particles. As the SOC decreased, more LFP particles were saturated, and the effective surface area decreased. Therefore, the C_p value during lithiation of LFP gradually decreased as the SOC decreased as shown in Fig. 2a. There was one extreme case when the SOC reached 10%. At this state, almost all particles were pure $FePO_4$, and the low concentration of Li-ions at the interfaces of particles would lead to a low C_p value.

Comparing Fig. 2a and b, we can see that the C_p value during delithiation was generally lower than that during lithiation. Under the LGPM conditions, the equivalent capacitance C_p is mainly contributed by the gradient of the concentration of the ions, and its value is largely determined by the rate of migration

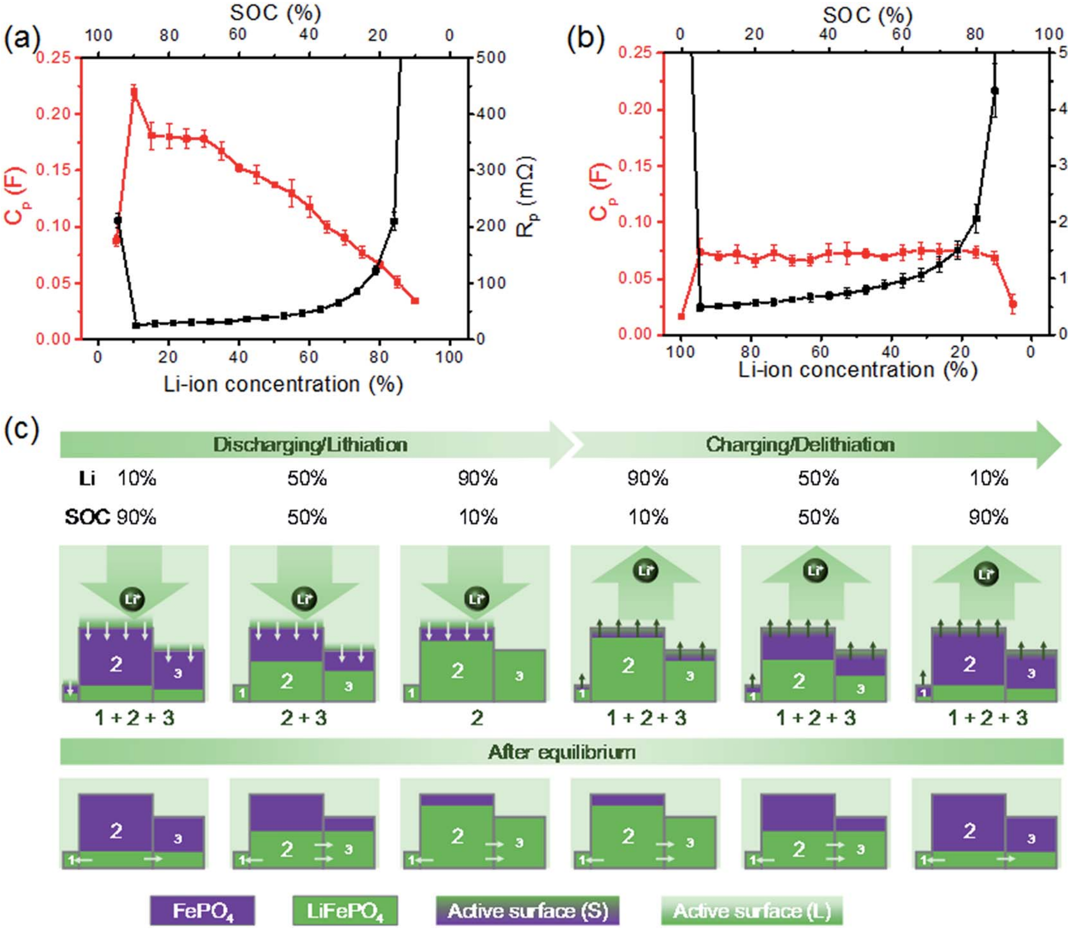

Fig. 2 The C_p and R_p curves of fresh LFP half-cells during (a) charging and (b) discharging; (c) effective surface area during charging and discharging.

of the ions. Qualitatively, faster migration will lead to less concentration gradient, or lower concentration polarization, and sequentially it will result in a higher C_p in the equivalent circuit. During lithiation, Li-ions migrated from the surface into the bulk in the LFP particles and they migrated reversely during delithiation. Since the absolute value of C_p during lithiation was generally higher than that during delithiation, we can postulate that Li-ions migrated faster from the surface to the bulk than the reversed direction.

The dependence of R_p on SOC was likely due to the reconstruction of the LFP/electrolyte interface during the extraction/insertion or solvation/desolvation of the Li-ions. At SOC around 100%, the LFP (mostly $LiFePO_4$)/electrolyte interface had not been completely reconstructed for ion transportation, and resistance for the extraction/insertion of Li-ions would be high so the R_p value would be high as well. Once the interface was established for easy transportation of the Li-ions, the R_p value decreased significantly. At a high SOC (>90%), the LFP (mostly $FePO_4$)/electrolyte interface was reconstructed and the transport of Li-ions was slowed down again, leading to R_p to decrease. Since the extraction of Li-ions from LFP was slower than the insertion, R_p was higher during delithiation.

In situ probing of interface of C_p and R_p and the Li-ion status of graphite microparticles

Fig. 3a and b show the C_p curves during the insertion and extraction process of Li-ions with graphite. The change of C_p *vs.* SOC was not significant and the shape of these two curves showed a certain degree of symmetry. Different from LFP, the effect of the particle size on the electrochemical potential in graphite has not been previously observed. Therefore, we assumed that particles of all sizes should be lithiated and delithiated simultaneously.

Differently, the graphite surface was covered by a SEI layer which can be easily traversed by Li-ions and is considered a good Li-ion conductor and charge buffer. Since the effective surface area was contributed by particles of all sizes, independent of SOC, the change of C_p *vs.* SOC was not significant. C_p reached the maximum value at SOC between 20% and 60% and it gradually decreased when the SOC was lower than 20% or higher than 60%. It appeared that either insertion or extraction of Li-ions in graphite was slower when the graphite was either almost empty or almost full. When the graphite was almost empty, the charge transfer was first taking place at the interface between the electrolyte and the SEI layer. As the graphite was filled with Li-ions, the charge transfer took place at both the

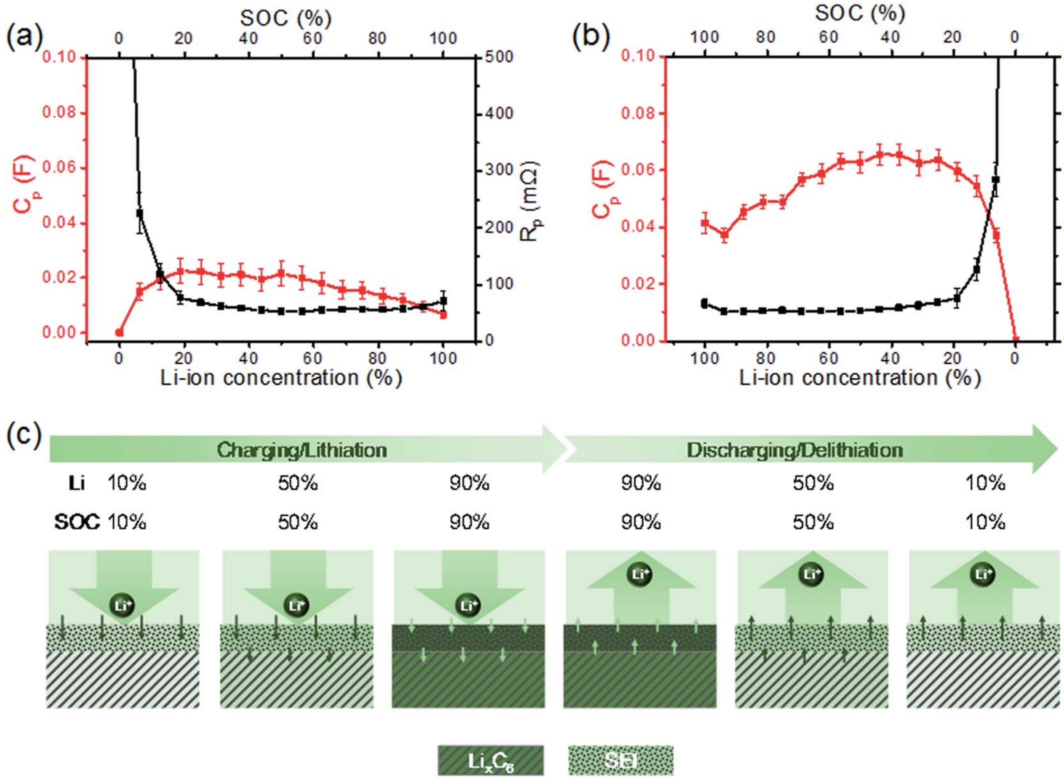

Fig. 3 The C_p and R_p curves of fresh graphite half-cells during (a) charging and (b) discharging; (c) SEI layer as a Li-ion buffer during charging and discharging.

interface between the electrolyte and the SEI layer, and the interface between the SEI layer and the graphite. As illustrated in Fig. 3c. Apparently, the exchange at the interface between the electrolyte and the SEI layer was much faster than that at the interface between the SEI layer and the graphite. The difference between these two interfaces caused the change of C_p at different SOCs.

Comparison between the C_p value during charging and discharging, we can notice that C_p was higher during discharging (delithiation). It suggests that the extraction of Li-ions was faster in comparison to the insertion of Li-ions, contrary to the case of LFP. During lithiation, the interlayer space of the graphite needed to be pushed apart to allow the insertion of Li-ions and the insertion process would be slower. The R_p curves during charging and discharging are also quite symmetrical, suggesting that there was not an interface reconstruction process for the graphite. The R_p curves can be seen in Fig. S10c and d.†

At the same time, we found that the error of C_p for graphite half-cells was larger than that of LFP half-cells. This was probably caused by the unstable SEI on the graphite half-cells. The formation and decomposition of the SEI layer during delithiation also contributed to the higher C_p value compared to lithiation. Because this method can get information on the interface between the electrode and the electrolyte, we believe that it can be used to analyse the SOH and SOC of LFP/graphite batteries.

Comparison between the C_p and R_p of LFP and graphite

The C_p value of the LFP/Li half-cells was about two to five times of that of the graphite/Li half-cells, and the difference was likely caused by the difference in the particle size. The primary particles of LPF were nanometer-sized, and the graphite particles were micrometer-sized, and the effective surface area of LFP would be higher and hence a higher C_p. However, the difference in C_p was not as significant as the difference in the particle size. It can be inferred that the faster diffusion of Li-ions in graphite than in LFP compensated for the significant difference between the particle sizes of these two materials.

In situ probing of interface of C_p and R_p and the Li-ion status of full LFP/graphite batteries

In order to research the performance of full batteries, we used the LGPM and the first-order equivalent circuit to study the 32650 LFP/graphite batteries (Fig. 4b). We chose two kinds of full batteries with different SOHs, which exhibited wide capacity difference at different current densities as shown in Fig. 4a. The unhealthy battery (UB) exhibited worse rate performance compared with the healthy battery (HB). We applied the LGPM and the equivalent circuit model to measure and analyzed the results, and obtained C_p (Fig. 4c and d) and R_p (Fig. S11†) during charging and discharging.

In order to identify the capacitance of the LFP/graphite batteries, EIS of the batteries was measured. The equivalent electrical circuit model is shown in Fig. S12,† and the

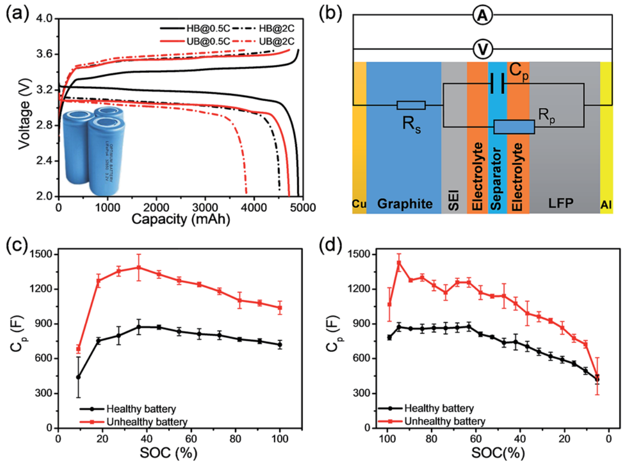

Fig. 4 (a) The rate performance of healthy and unhealthy LFP/graphite batteries at different current densities; (b) the battery healthy model; the C_p curves of the healthy and unhealthy batteries during (c) charge and (d) discharge.

comparison of measured and simulated spectra of the LFP/graphite battery can be seen in Fig. S13.† The fitting results and curve can be seen in Table S3.† In the fitting results we can found that the EDLC was only about 3.972 F. There is a big difference between the EDLC and C_p. In the LGPM test, the pulse lasted ten seconds. The lowest frequency in the EIS test was 0.01 Hz. Therefore physically C_p cannot be represented by the EDLC or Warburg element.

According to our previous study, the R_s of the HB and UB overlaps.[30] It was difficult to use R_s and R_p for battery diagnosis. Obviously, the C_p curves show a big difference between the HB and UB both in the charge and discharge processes (see Fig. 4c and d). So we can estimate the SOH at different SOCs of LFP/graphite LIBs using the C_p curves during charging and discharging, but the underlying cause leading to the above difference was unclear.

Ex situ structural analysis of the electrodes and degradation mechanism

Based on the above findings, we unpacked two kinds of full batteries and packed them into new batteries with Li metal. Then we did measurements using the LGPM, and obtained the C_p and R_p of the four types of half-cells as shown in Fig. 5 and S14.† The capacitance of LFP electrodes taken from the HB and UB in half cells was similar (no significant difference considering measurement errors) both in charge and discharge processes as shown in Fig. 5a and b. The LFP particles from the HB and UB were similar under SEM (Fig. S15†) with clean surfaces, from which we can infer that the LFP was not the main reason for battery degradation. In contrast, the graphite anode from the UB formed a thicker SEI layer with larger surface roughness than that from the HB (Fig. 6 and Table S4†). With the thicker SEI layer on the electrode surface, the graphite electrode from the UB showed a higher capacitance than that from the HB as shown in Fig. 5c and d. As previously

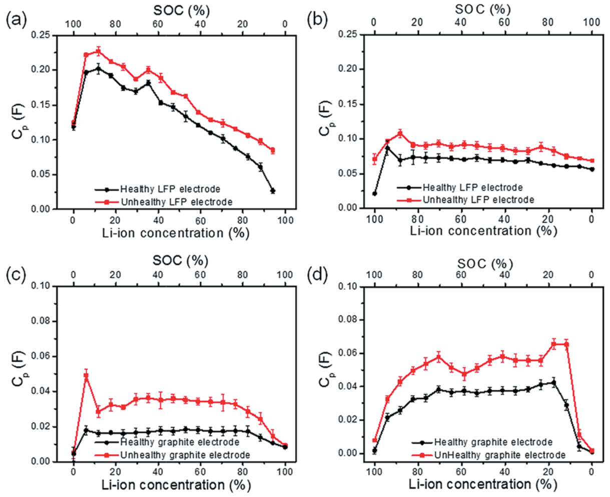

Fig. 5 The C_p curves of LFP half-cells made from healthy and unhealthy LFP electrodes at different SOCs during (a) lithiation and (b) delithiation; the C_p curves of graphite half-cells made from healthy and unhealthy graphite electrodes at different SOCs during (c) lithiation and (d) delithiation.

mentioned, the SEI layer has two interfaces, *i.e.* the graphite/SEI and the SEI/electrolyte interfaces. During charging/discharging, the SEI layer acted as a secondary Li-ion storage in the battery. A thicker SEI was able to store more Li-ions, and reduced the number of Li-ions stored in the graphite, leading to reduced Li capacity. Since Li-ions migrate faster in the SEI layer than in the graphite, a thicker SEI layer showed a higher C_p value.

When we compare the capacitance of LFP and graphite half-cells shown in Fig. 5a and b, we can find that the capacitance of LFP electrodes is about 3 times larger than that of graphite electrodes, after being normalized to the Li-ion capacity. The big difference in the capacitance between the electrode was due to the particle size difference between LFP and graphite (Fig. S17†). So the C_p curves in Fig. 4c and d are more dominated by the capacitance of the graphite electrode. However, the main

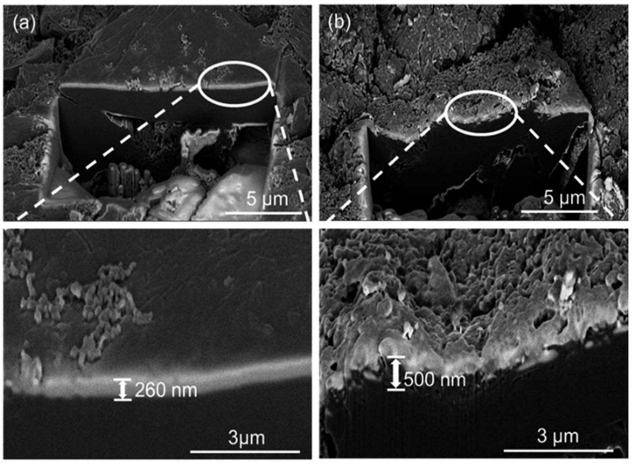

Fig. 6 The SEM images of the (a) healthy and (b) unhealthy graphite electrode.

reason leading to the unhealthy condition of all batteries was the destruction of the graphite electrode. On the whole, we can estimate the SOH of used batteries by judging from the C_p curves. In order to verify the validity of our hypothesis, we made LFP and graphite half cells using electrodes recovered from unhealthy batteries and tested them with a large current step. According to the voltage respond curves, we obtained the C_p and R_p of LFP and graphite half-cells using the model shown in Fig. 1a. Then we put these parameters into the equivalent circuit diagram (Fig. S18†) and obtained the estimated C_p and R_p of full batteries. The trajectory of estimated C_p and R_p and the relationship between the response curve and the estimated data are shown in Fig. S19 and S20.† We compared the R_p and C_p data with the estimated values as shown in Fig. S20.† Obviously, the estimated curves were similar to the C_p and R_p curves of the graphite, which suggests that the deterioration of the graphite electrode was responsible for the degradation of the full battery.

Conclusions

In this work, we demonstrated that the SOH and SOC of LFP/C batteries can be probed *in situ* using a large galvanostatic pulse method (LGPM) in combination with a simple first-order RC equivalent circuit. By applying a large step current, fitting the voltage response during the transient process can supply information about the change of the effective surface area as reflected by the change of the equivalent capacitance. With additional *ex situ* analysis of the morphology of the electrodes, we can relate the SOH of the battery to the value of C_p. We found that a higher C_p suggests an unhealthy battery, and the C_p can also be used to estimate the SOC given a C_p *vs.* the SOC curve is measured beforehand. In addition, we identify that the graphite anode has more responsibility for the degradation of the full batteries by analyzing the LFP cathode and the graphite anode separately. The LGPM and the equivalent circuit model demonstrated in this work can potentially become a practical tool for *in situ* probing the interfacial kinetics for studying the electrochemical properties of active particles and for online and real-time measurement of the SOC and SOH of LFP/C batteries in actual systems. When a vehicle is starting or accelerating, the motor draws a significant current from the battery and it can last several seconds. The voltage response can be recorded with a sample rate no less frequent than 5 Hz. A least square method is carried out by the programmed MCU using eqn (2). The equivalent capacitance and parallel resistance values can be calculated and correlated with an SOH value using pre-stored relationships.

Conflicts of interest

The authors declare no competing financial interest.

Acknowledgements

The research was financially supported by the Guangdong Innovation Team Project (No. 2013N080), Shenzhen Science and Technology Research Grant (No. JCYJ20151015162256516, JCYJ20150729111733470), and International cooperation project of Shenzhen science and technology research and development funds (No. GJHZ20160229122304608).

Notes and references

1 J. M. Tarascon and M. Armand, *Nature*, 2001, **414**, 359–367.
2 T. Sarıkurt, M. Ceylan and A. Balıkçı, *presented at the 2014 IEEE International Energy Conference (ENERGYCON)*, Dubrovnik, Croatia, 2014.
3 W. G. H. Martin Coleman and C. K. Lee, *IEEE Transactions on Energy Conversion*, 2008, **23**, 708–713.
4 S. J. Moura, N. A. Chaturvedi and M. Krstić, *J. Dyn. Syst., Meas., Control*, 2013, **136**, 011015.
5 Y. Zou, X. Hu, H. Ma and S. E. Li, *J. Power Sources*, 2015, **273**, 793–803.
6 A. Barre, B. Deguilhem, S. Grolleau, M. Gerard, F. Suard and D. Riu, *J. Power Sources*, 2013, **241**, 680–689.
7 M. Berecibar, I. Gandiaga, I. Villarreal, N. Omar, J. Van Mierlo and P. Van den Bossche, *Renewable Sustainable Energy Rev.*, 2016, **56**, 572–587.
8 Z. Chen, C. C. Mi, Y. Fu, J. Xu and X. Gong, *J. Power Sources*, 2013, **240**, 184–192.
9 A. Eddahech, O. Briat, N. Bertrand, J.-Y. Deletage and J.-M. Vinassa, *Int. J. Electr. Power Energy Syst.*, 2012, **42**, 487–494.
10 B. Saha, K. Goebel and J. Christophersen, *Trans. Inst. Meas. Control*, 2009, **31**, 293–308.
11 C. Zou, C. Manzie, D. Nesic and A. G. Kallapur, *J. Power Sources*, 2016, **335**, 121–130.
12 P. Arora, M. Doyle, A. S. Gozdz, R. E. White and J. Newman, *J. Power Sources*, 2000, **88**, 219–231.
13 E. Martínez-Rosas, R. Vasquez-Medrano and A. Flores-Tlacuahuac, *Comput. Chem. Eng.*, 2011, **35**, 1937–1948.
14 M. Safari and C. Delacourt, *J. Electrochem. Soc.*, 2011, **158**, A63–A73.
15 V. Srinivasan and J. Newman, *J. Electrochem. Soc.*, 2004, **151**, A1517–A1529.
16 M.-L. Lee, Y.-H. Li, S.-C. Liao, J.-M. Chen, J.-W. Yeh and H. C. Shih, *Appl. Surf. Sci.*, 2012, **258**, 5938–5942.
17 T. K. Dong, A. Kirchev, F. Mattera, J. Kowal and Y. Bultel, *J. Electrochem. Soc.*, 2011, **158**, A326.
18 H. He, R. Xiong and J. Fan, *Energies*, 2011, **4**, 582–598.
19 H. He, R. Xiong and H. Guo, *Appl. Energy*, 2012, **89**, 413–420.
20 S. J. Lenhart, *J. Electrochem. Soc.*, 1988, **135**, 1063.
21 P. L. Moss, G. Au, E. J. Plichta and J. P. Zheng, *J. Electrochem. Soc.*, 2008, **155**, A986.
22 S. M. Mousavi G. and M. Nikdel, *Renewable Sustainable Energy Rev.*, 2014, **32**, 477–485.
23 D. Riu, M. Montaru and Y. Bultel, *Comm. Nonlinear Sci. Numer. Simulat.*, 2013, **18**, 1454–1462.
24 R. Xiong, H. He, H. Guo and Y. Ding, *Procedia Eng.*, 2011, **15**, 2869–2874.
25 A. Fotouhi, D. J. Auger, K. Propp, S. Longo and M. Wild, *Renewable Sustainable Energy Rev.*, 2016, **56**, 1008–1021.
26 S. Nejad, D. T. Gladwin and D. A. Stone, *J. Power Sources*, 2016, **316**, 183–196.

27 J. Lu, Z. Chen, Z. Ma, P. Feng, L. A. Curtiss and K. Amine, *Nat. Nanotechnol.*, 2017, **12**, 90.

28 J. Hu, Y. Jiang, S. Cui, Y. Duan, T. Liu, H. Guo, L. Lin, Y. Lin, J. Zheng and K. Amine, *Adv. Energy Mater.*, 2016, **6**, 1600856.

29 L. R. F. A. J. Bard, *Electrochemical Methods: Fundamentals and Applications*, John wiley & Sons, Inc, 2nd edn, 2001.

30 R.-X. Qiao, M.-J. Zhang, Y.-D. Liu, W.-J. Ren, Y. Lin and F. Pan, *Chin. Phys. Lett.*, 2016, **33**, 078201.

31 K. T. Lee, W. H. Kan and L. F. Nazar, *J. Am. Chem. Soc.*, 2009, **131**, 6044–6045.